Supplementary Materials for

Spectral narrowing of x-ray pulses for precision spectroscopy with nuclear resonances

K. P. Heeg, A. Kaldun, C. Strohm, P. Reiser, C. Ott, R. Subramanian, D. Lentrodt, J. Haber, H.-C. Wille, S. Goerttler, R. Rüffer, C. H. Keitel, R. Röhlsberger, T. Pfeifer, J. Evers*

*Corresponding author. Email: joerg.evers@mpi-hd.mpg.de

Published 28 July 2017, *Science* **357**, 375 (2017)
DOI: 10.1126/science.aan3512

This PDF file includes:

Theory

A general framework to compute the x-ray field after interaction with moving targets was developed in Ref. (*31*). Let us assume a general initial field $E_{\text{in}}(t)$. Its interaction with the resonant nuclei can best be described in the rest frame of the target. For non-relativistic velocities, the x-ray field in the rest frame is $\tilde{E}_{\text{in}}(t) = E_{\text{in}}(t)\exp(-ikx(t))$, where $x(t)$ is the motion of the target in the laboratory frame and k is the wave number. Its Fourier transform $\tilde{E}_{\text{in}}(\omega)$ is the field in frequency space. For the output field we have $\tilde{E}_{\text{out}}(\omega) = \tilde{E}_{\text{in}}(\omega)\,T(\omega)$, where $T(\omega)$ is the complex transmission function of the target at rest. The transmission functions $T(\omega)$ used in our simulations were computed using the software package CONUSS (*32*) and include the respective realistic material properties. Denoting the inverse Fourier transform of $T(\omega)$ as $E(t)$, we can alternatively compute the final x-ray field in the piezo frame $\tilde{E}_{\text{out}}(t)$ via the convolution $\tilde{E}_{\text{in}}(t) * E(t)$. Transforming the field back into the laboratory frame, we have $E_{\text{out}}(t) = \tilde{E}_{\text{out}}(t)\exp(ikx(t))$. Note that this theory naturally covers the interaction of the x-ray field with the slow-moving Mössbauer drive as well.

In the following, we discuss the special case of a very short incident pulse in more detail. This is the situation encountered for a synchrotron pulse, which is interacting with the first target. Since the x-ray pulse is short compared to the nuclear lifetime, it can be well approximated by the Dirac δ function,

$$E_{\text{in}}(t) \sim \delta(t)\ . \tag{S1}$$

In the rest frame of the target, the field becomes $\tilde{E}_{\text{in}}(t) = \delta(t)\exp(-ikx(0))$. Next, the interaction with the target leads to the outgoing field $\tilde{E}_{\text{out}}(t) = [\delta(t)\exp(-ikx(0))] * E(t) = E(t)\exp(-ikx(0))$. Finally, after transformation back into the laboratory frame, the x-ray field becomes

$$E_{\text{out}}(t) = E(t)e^{ik[x(t)-x(0)]}\ . \tag{S2}$$

Up to a global phase, this constitutes the target response function $E(t)$ modulated with the displacement phase $\exp(ikx(t))$, as illustrated in Fig. 1 in the main text.

For the case of a single-line resonance in the resonant nuclei, the response function $E(t)$ can be expressed analytically. This case is realized, e.g., for a stainless steel foil with resonant ^{57}Fe nuclei. We have (*31*)

$$E(t) = \delta(t) - \sqrt{\frac{b}{t}}J_1\left(2\sqrt{bt}\right)e^{-\gamma t/2}e^{-i\omega_0 t}\theta(t)\ , \tag{S3}$$

where ω_0 is the resonance frequency, γ the width, and

$$b = \frac{1}{4}\gamma\sigma_0 f_{\text{LM}} n d \tag{S4}$$

parametrizes the thickness of the target with resonant cross section σ_0, Lamb-Mössbauer factor f_{LM}, number density n and thickness d. $\theta(t)$ denotes the Heaviside step function and J_1 is the

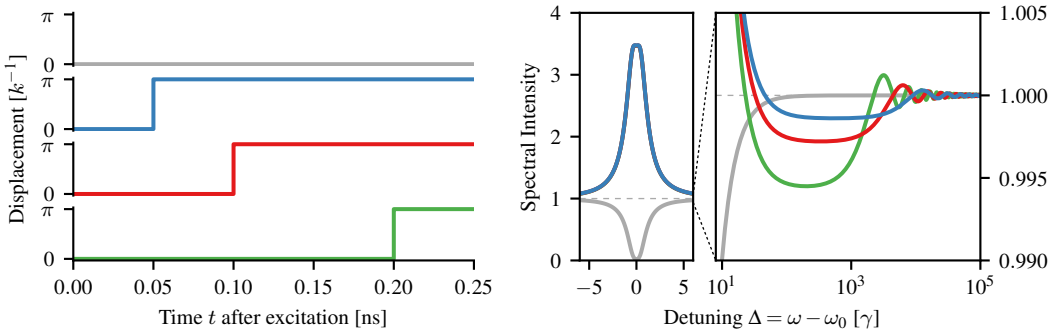

Figure S1: Energy conservation, and effect of the delay between excitation and phase jump. The left panel shows four idealized phase evolutions induced by the piezoelectric transducer. The gray curve is a reference without motion. In all three other cases, a phase jump of π is applied, but at different delays after the excitation. The right panel shows corresponding spectra, normalized to the input pulse spectrum. Electronic absorption is neglected for clarity. Without motion, an absorption dip around nuclear resonance can be observed, whereas for the cases with motion, essentially the same resonant enhancement is seen. The far off-resonant behavior is shown on a logarithmic scale on the right. Note that only a tiny intensity range around the normalized input pulse spectrum is shown. With motion, the intensity drops below that of the input pulse in a certain range, indicating spectral redistribution and energy conservation. The results are obtained for a single-line stainless steel absorber with thickness parameter $b = \gamma$.

Bessel function of the first kind. If the target is driven by a $\delta(t)$-like pulse, the temporal response becomes

$$E_{\text{out}}(t) = \delta(t) - \sqrt{\frac{b}{t}} J_1\left(2\sqrt{bt}\right) e^{-\gamma t/2} e^{-i\omega_0 t} e^{ik[x(t)-x(0)]} \theta(t) \,, \tag{S5}$$

and for the (normalized) spectral composition we have

$$\begin{aligned} E_{\text{out}}(\omega) &= \int E(t)\, e^{ik[x(t)-x(0)]}\, e^{i\omega t}\, dt \\ &= 1 - \int_0^\infty \sqrt{\frac{b}{t}} J_1\left(2\sqrt{bt}\right) e^{-\gamma t/2} e^{-i(\omega_0-\omega)t} e^{ik[x(t)-x(0)]} dt \,. \end{aligned} \tag{S6}$$

For a near-instantaneous displacement $kx = \pi$, the translational phase $e^{ik[x(t)-x(0)]}$ becomes -1, except at $t = 0$. Since the latter case has measure zero in the integral, we can approximate $e^{ik[x(t)-x(0)]} = -1$ and evaluate the integral. We obtain

$$E_{\text{out}}(\omega) \approx 2 - \exp\left(\frac{-ib}{\omega - \omega_0 + i\frac{\gamma}{2}}\right) . \tag{S7}$$

It is easily seen that this expression approaches unity for off-resonant frequencies and exceeds the input spectrum around the resonance.

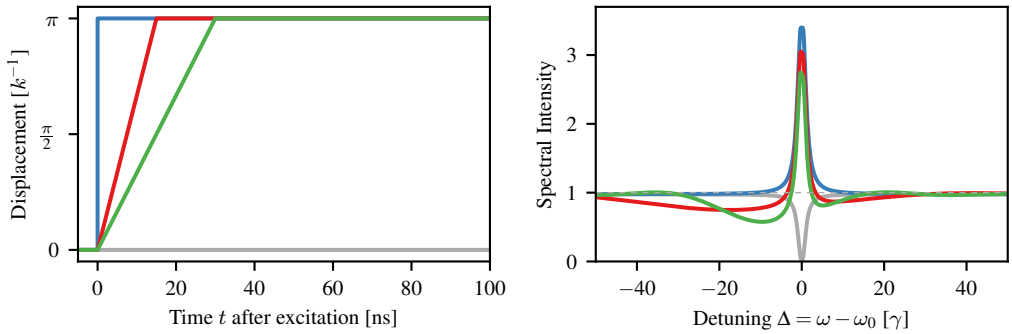

Figure S2: Effect of non-instantaneous phase shifts on the enhancement mechanism. The left panel shows three idealized phase evolutions induced by the piezoelectric transducer, as function of time. The blue curve corresponds to an instantaneous phase jump, while the red and green trajectories model phase shifts in different finite times. The right panel shows the corresponding spectra. All motional patterns lead to substantial enhancement on resonance. The instantaneous jump harvests an invisibly small amount of intensity at all frequencies of the entire spectrum. The finite-time phase shifts harvest in smaller spectral regions, with width inversely proportional to the shift time. Furthermore, the linear phase evolution corresponds to a Doppler shift, which moves the center of the harvesting area away from resonance. The gray curve in the right panel shows the spectrum without motion as a reference. The results are obtained for a single-line stainless steel absorber enriched to 95% in ^{57}Fe with thickness parameter $b = \gamma$ (corresponding to a physical thickness of about 0.45 μm).

Spectral redistribution

In the derivation of Eq. (S7) an approximation in the translational phase was performed, such that the integral could be solved analytically. In this case, it is apparent that energy conservation is violated, as the total x-ray intensity exceeds that of the input field. However, a full calculation reveals that spectral intensity is redistributed from off-resonant frequencies onto resonance, thus satisfying energy conservation. This is illustrated in more detail in Fig. S1, where different displacements $kx = \pi$ at near-instantaneous times after excitation are considered. Computing the normalized spectral intensity according to Eq. (S6), one observes the spectral boost on resonance. For off-resonant frequencies, however, the intensity drops below unity, indicating the range from where spectral energy is harvested and redistributed onto resonance. This important mechanism was not captured by the simplified analysis leading to Eq. (S7). With decreasing time delay between excitation and displacement, this range becomes broader and at the same time the absorption due to the harvesting decreases. In the limit of zero delay, resonant enhancement is achieved via vanishing additional absorption over the infinite spectral range of the entire spectrum and the spectral intensity approaches the estimate from Eq. (S7), while energy conservation remains satisfied.

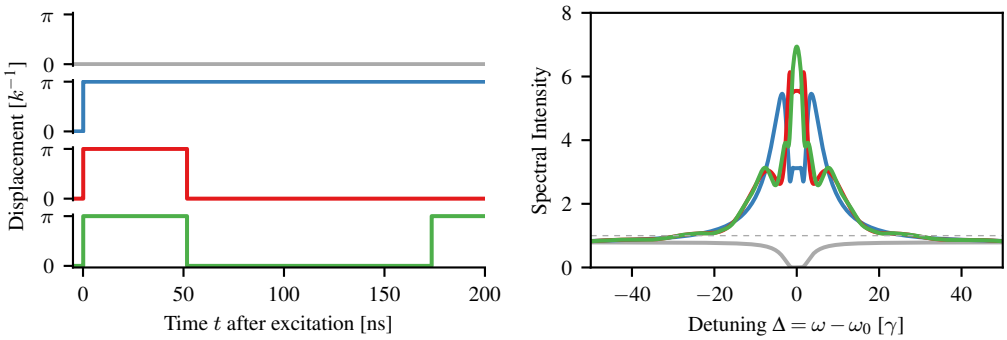

Figure S3: Optimum motional pattern. The left panel shows four different phase evolutions. The first one (gray curve) is for the case without motion. The subsequent ones have a phase shift by π immediately after the excitation. They differ in that they have no further phase shifts (blue), or a π phase shifts in the next (red), or in the two following roots (green) of the Bessel function (the so-called dynamical beats), see Eq. (S8). In the right panel, the corresponding spectra are shown. It can be seen that without phase shift, the usual absorption curve is obtained. With phase shifts, in all cases enhancement is achieved. However, the enhancement is optimized by increasing the number of phase jumps. The results are obtained for a single-line stainless steel absorber enriched to 95% in ^{57}Fe with thickness parameter $b = 10\gamma$ (corresponding to a physical thickness of about 4.5 μm). Note that energy-conservation is satisfied in all spectra, via the mechanism illustrated in Fig. S1.

Non-instantaneous displacements

An instantaneous displacement of a resonant target as considered above is not viable in a realistic setting. Instead, it requires a finite amount of time. The effect of such displacement durations is studied in Fig. S2. Next to an instantaneous phase jump, two motions with a finite ramping time are considered. It can be observed that the spectral enhancement on resonance is still present, however, its amplitude decreases with larger displacement times. The finite-time phase shifts give rise to harvesting in a spectral range with width inversely proportional to the shift time, which for the instantaneous jump results in an invisibly small amount of intensity (see previous section) at all frequencies of the entire spectrum. The linear displacement is associated with a Doppler shift, which determines the position of the harvesting center. In all cases, though, the mechanism responsible for the spectral boost on resonance is the displacement by $\lambda/2$, not the Doppler shift due to the finite displacement time.

Upper limit of the spectral boost

Below, we determine the maximum spectral intensity which can be obtained with our method. For simplicity, we consider the case of a single-line resonance again, since the transmission function of the target possesses an analytical expression (Eq. (S3)).

In a first step, we determine the normalized spectral intensity behind a single piezo target,

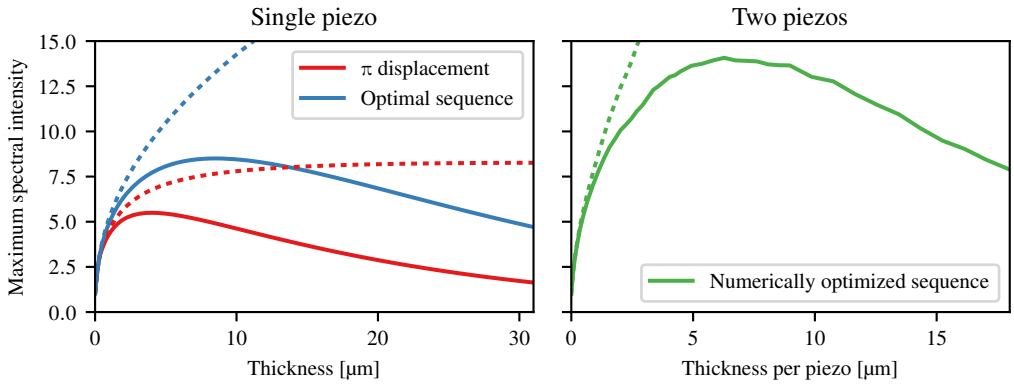

Figure S4: Theoretical limit of the spectral boost. In the left panel, the maximum spectral intensity which can be achieved with a single target on a piezo is shown. The result for a prompt displacement of $kx = \pi$ immediately after the excitation is shown in red, the ultimate limit as determined in Eq. (S9) is shown in blue. Electronic absorption is [included/neglected] in the [solid/dashed] lines. Results for two piezos, obtained with a Monte-Carlo optimization, are shown in the right panel. All computations were performed for a single-line stainless steel target, whose iron component is enriched to 95% in the resonant isotope ^{57}Fe.

driven by a synchrotron pulse. From Eq. (S6) we find

$$\begin{aligned} I(\omega) &= |E_{\text{out}}(\omega)|^2 \\ &\leq \left(1 + \left|\int_0^\infty dt \sqrt{\frac{b}{t}} J_1\left(2\sqrt{bt}\right) e^{-\gamma t/2} e^{-i(\omega_0-\omega)t} e^{ik[x(t)-x(0)]}\right|\right)^2 \qquad \text{(S8)} \\ &\leq \left(1 + \int_0^\infty dt \sqrt{\frac{b}{t}} \left|J_1\left(2\sqrt{bt}\right)\right| e^{-\gamma t/2}\right)^2 \equiv I_{\text{opt}}\,, \qquad \text{(S9)} \end{aligned}$$

where the first "$\leq$" is due to $|\alpha + \beta| \leq |\alpha| + |\beta|$, and the second due to the generalization $|\int f(t)dt| \leq \int |f(t)|dt$. A comparison of Eqs. (S8) and (S9) shows that the optimum harvesting intensity I_{opt} can in fact be realized on resonance $\omega = \omega_0$. For this, $x(t)$ must be chosen in such a way that it cancels the sign flips of the Bessel function J_1 for all times t. This can be achieved if $x(t)$ jumps once by $(2n+1)\lambda/2$ immediately after the excitation, and subsequently again at each sign flip of $J_1(2\sqrt{bt})$. This is illustrated in more detail in Fig. S3. For an increasing number of jumps the spectral intensity on resonance $I(\omega_0)$ approaches the optimum I_{opt}. For targets of moderate thickness, a single jump immediately after the excitation well approximates the optimum jump sequence.

The maximum spectral boost increases continuously with the thickness parameter b, however at the same time the electronic non-resonant absorption increases as well. Both effects lead to an optimum sample thickness, at which the highest spectral intensity can be achieved. Consequently, a strong nuclear scattering connected with small electronic absorption, as it is

the case for samples enriched in their resonant isotope, is beneficial. In Fig. S4 we illustrate the maximally achievable spectral amplification for the case of a stainless steel target, enriched in ^{57}Fe. It can be seen that a maximum enhancement of approximately 8 is obtained. Similar calculations show that for the case of a α-Fe target, a maximum enhancement of about 12 can be achieved, due to the lower electronic absorption for the same number of resonant nuclei.

Next, let us briefly discuss the situation of multiple piezo stages. In those cases, the expression for the scattered light acquires a more complex time dependence due to the convolved piezo responses and a meaningful theoretical limit cannot be derived analytically anymore. Instead, for the case of two piezos, we performed numerical simulations and optimized the piezo motions via an evolutionary algorithm with the aim to increase the maximum spectral intensity. To this end, we allowed for up to five independent jumps in the position of the two piezos as function of time. This parametrization may not cover the optimum motions, but will certainly provide a reasonable lower limit of the maximally achievable spectral boost. The results are shown in the right panel of Fig. S4. It can be observed that the maximum performance of a single target can be easily beaten with two piezo stages.

Finally, we would like to comment on the limited longitudinal coherence of synchrotron or XFEL pulses. Using numerical simulations based on partially coherent x-ray pulses (*33*), we confirmed that the angular spectral coherence width σ_{coh} is inversely proportional to the temporal duration τ of the pulse, and the product $\tau\sigma_{coh}$ converged for a broad range of pulses with relevant durations and spectral widths to an universal constant of order 10. For a synchrotron pulse duration of $10 - 100$ ps, we thus estimate the coherence width to be of order 10^4 natural line widths of the ^{57}Fe resonance, such that the spectral coherence is not a limitation to our scheme for switching times on the nanosecond scale.

Samples

The piezoelectric transducers consist of a polyvinylidene fluoride (PVDF) film (thickness 28 and 52 μm, models DT1-028K/DT1-052K, Measurement Specialties, Inc.). The piezos were glued on a plexiglas backing and were driven by arbitrary-function generators (model Keysight 81160A-002). For the resonant nuclear targets, which were glued to the piezo films, we used α-iron foils with thicknesses of ≈ 2 μm, enriched to about 95% in ^{57}Fe. An external magnet was used to align the magnetization of the targets and the setup was arranged such that only the two $\Delta m = 0$ hyperfine transitions of the 14.4 keV resonance in ^{57}Fe were driven. The single-line analyzer used on the Mössbauer drive was a stainless steel foil, also enriched in ^{57}Fe and with thickness 1 μm. For all targets the temporal response after a prompt x-ray excitation was measured and from these time spectra the exact material properties could be determined with CONUSS (*32*). Only minor deviations from the projected two- and single-line targets due to isomer shift distributions were found.

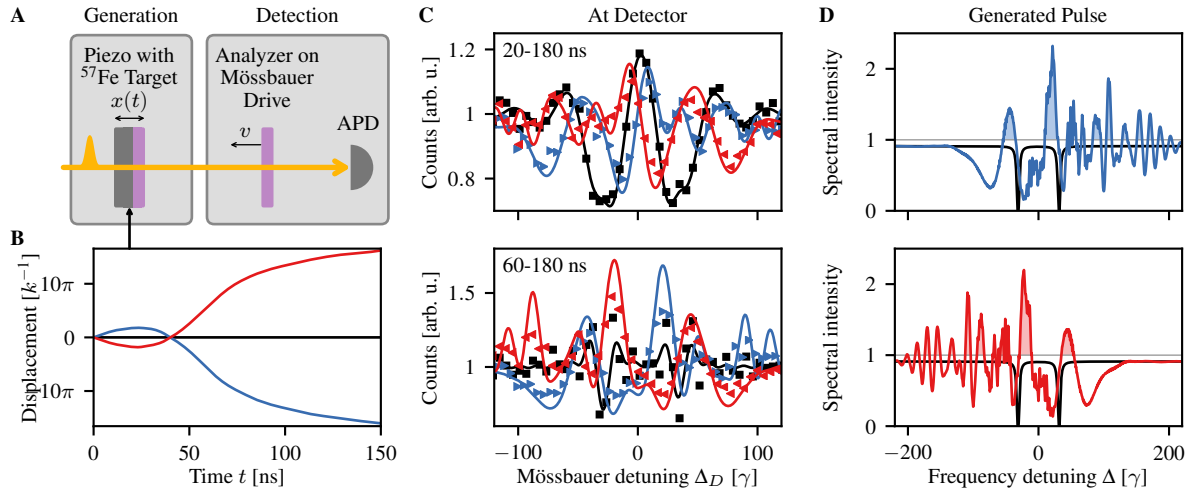

Figure S5: Tailoring the nuclear response over a wider spectral range. This figure shows results as in Fig. 2 of the main text, but for a different motional pattern of the piezo, measured at the High Resolution Dynamics Beamline P01 of PETRA III, DESY, Hamburg. It can be seen that the piezo motions with larger amplitude lead to strong manipulations of the spectrum over a range of about 200 natural linewidths, demonstrating the potential for further improvement of the resonant intensity enhancement or comprehensive x-ray spectral shaping.

Detection

The narrow linewidth of Mössbauer resonances associated with their high transition frequencies renders a direct x-ray pulse characterization challenging. For energy analysis of the radiation transmitted through the piezo target, we used a stainless steel foil, enriched in ^{57}Fe, acting as a single-line analyzer. It was mounted on a Doppler drive, where a constant motion with velocity v translates in a Doppler shift-induced detuning $\Delta_D = \omega_0 v/c$ of its resonance frequency relative to the nuclear transition. Scanning the Doppler detuning Δ_D across the ^{57}Fe resonance allowed us to record time- and energy-resolved spectra for the combined system of target and analyzer (see Refs. *(8, 13)*).

Reconstruction of the piezo motion

In the experiment our piezos were periodically driven by an arbitrary-function generator. However, they will in general not directly follow the applied pattern on fast time scales due to their inertia and due to signal dispersion and bandwidth limitations in the transmission from electric voltage to mechanical motion. We reconstructed their actual motion from the measured data as follows. Starting with a random piezo motion $x(t)$, the theoretically expected time- and energy-resolved spectrum is computed and compared with the measured data. An evolutionary algorithm is used to successively optimize $x(t)$ until the theoretical predictions converge to the

experimental data. Repeated applications of the method yield nearly identical results for the first 60 ns after excitation. To reconstruct the complete periodic motion, we recorded several datasets for which the respective moments of the x-ray excitation were temporally shifted in steps of less than 30 ns. Reconstructing the respective displacement fragments as explained above allows one to cover the complete period of the piezo displacement function $x(t)$. Overlapping ranges stemming from different reconstructions are in very good agreement and thus serve as a further cross-check of this reconstruction method.

Addressing a broader spectral range

Fig. S5 shows experimental results obtained for piezo motion of larger amplitude, recorded at the High Resolution Dynamics Beamline P01 of PETRA III, DESY, Hamburg (*34*). Like Fig. 2 in the main text recorded at the Nuclear Resonance Beamlime ID18 of ESRF, Grenoble (*35*), panel A shows the setup, and B the recovered motion. The piezo-induced displacements are more than one order of magnitude larger than those reported in Fig. 2 of the main text, due to a larger voltage applied to the piezo. As a consequence, the spectra shown in C, D are manipulated over a spectral range of about 200 natural linewidths.

Additional measurements

Additional experimental data for the cases shown in Figs. 2 and 3 in the main text and in Fig. S5 are presented in Fig. S6. The time- and energy resolved spectra integrated over a larger number of time ranges are shown, together with theoretical fits. The good agreement over the full time span indicates that the reconstruction of the motion of the samples is reliable. As explained in the main text, theory curves for Fig. S6C are computed using only the single-piezo results.

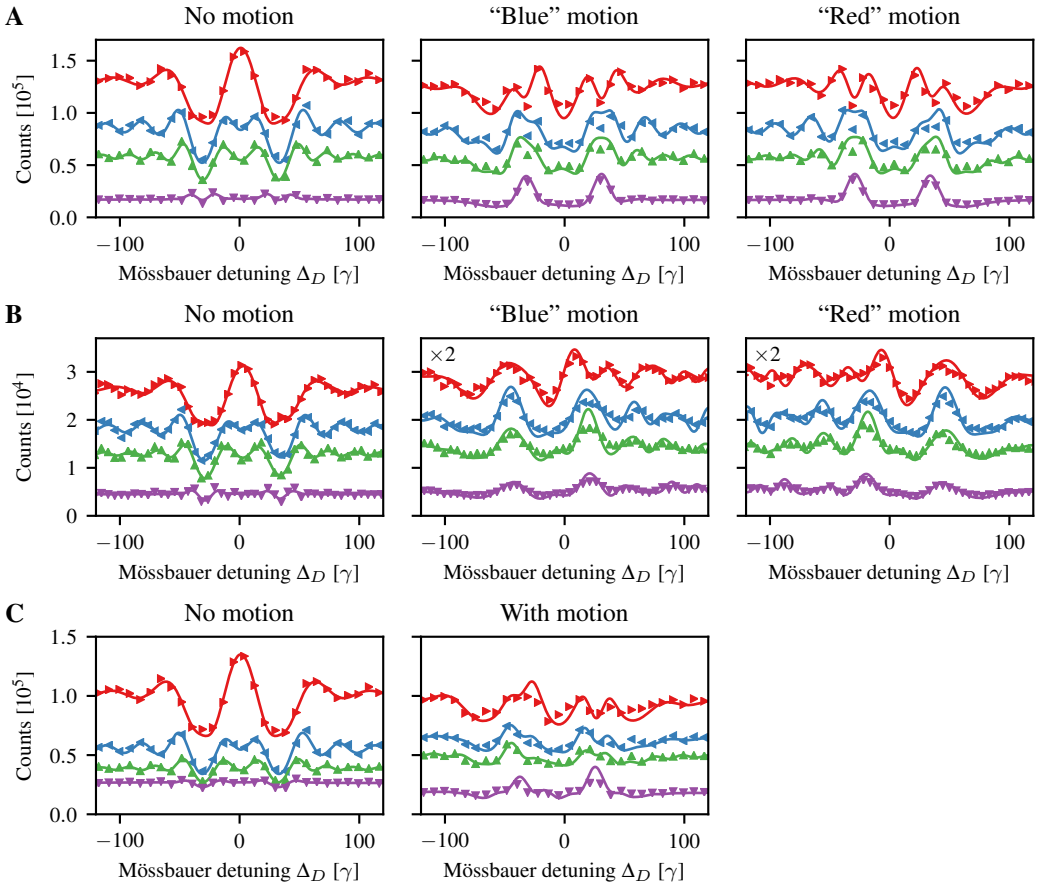

Figure S6: Additional measurements. Time- and energy resolved spectra integrated over different time ranges (markers) are shown together with theoretical fits (solid lines). In each panel in **A** and **C** the time ranges from top to bottom are [20, 30, 40, 60] to 168 ns, in **B** the ranges extend to 180 ns. Photon shot noise errors are within the marker size. **A** Single-piezo measurements at ESRF with motions "blue" and "red" as in Fig. 2 in the main text. **B** Single-piezo measurements at PETRA III (DESY) with motions "blue" and "red" as in Fig. S5. **C** Two-piezo measurements at ESRF with motion as in Fig. 3 in the main text.

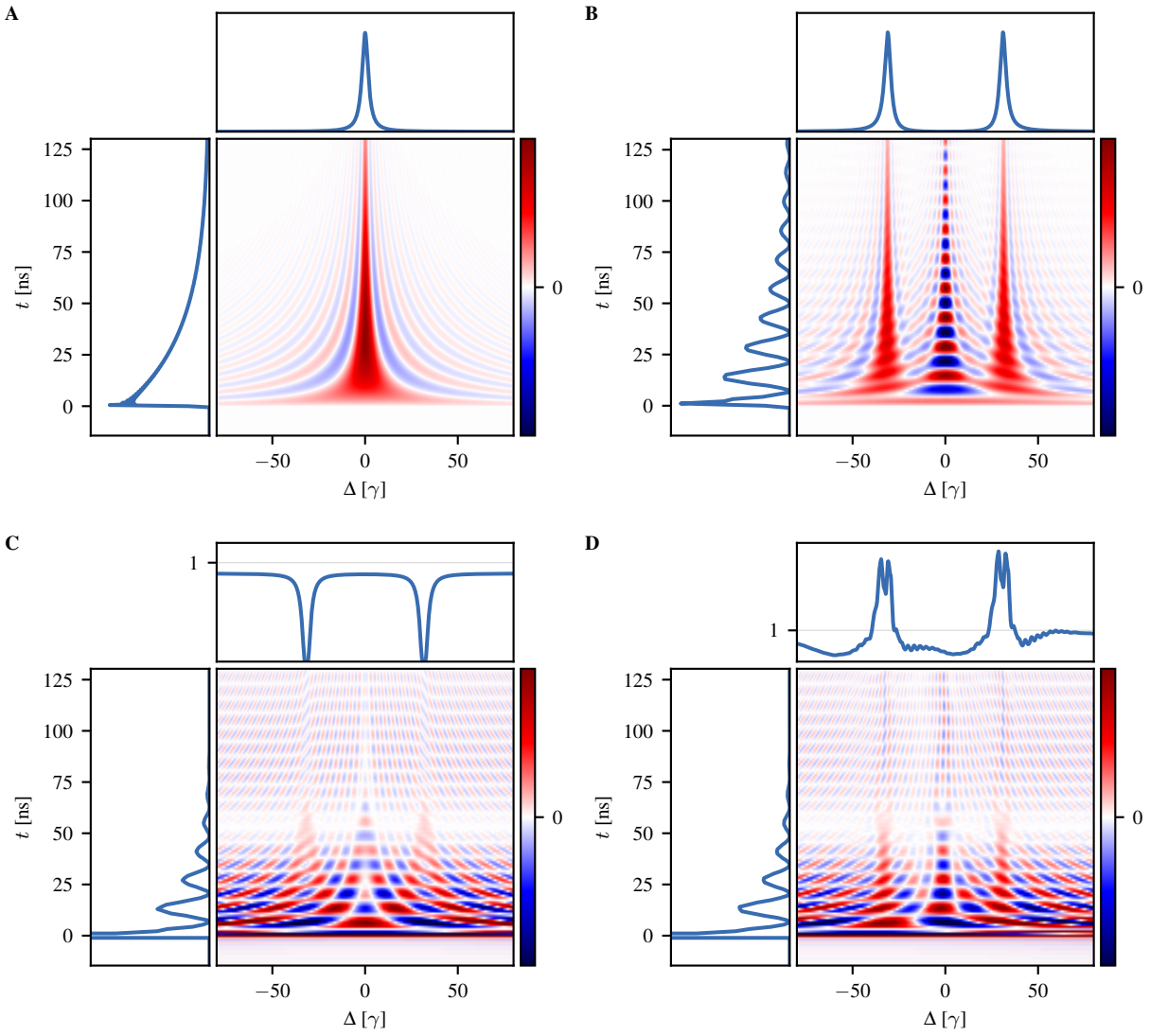

Figure S7: Wigner representation of the x-ray field. Panels **A** and **B** show the theoretical Wigner representations $W(t,\Delta) = \int E(t+\frac{\tau}{2})E(t-\frac{\tau}{2})^* \exp(i\Delta\tau)d\tau$ of a Lorentzian pulse and of a double-Lorentzian pulse with splitting 62γ, respectively. It can be seen that the coherence of the two contributions in **B** results in a pronounced interference pattern around $\Delta = 0$. In **C** and **D** the reconstructed Wigner representations of the measured x-ray pulses are shown. Data shown in **C** involves no motion of the target, while **D** corresponds to the pulse shown in the upper panel of Fig. 2D in the main text, for which a strong enhancement at the resonances was achieved. The similarity of **B** and **D** is well visible. In all panels the projections along the time- and frequency axes are shown in addition.

References

1. M. Kalvius, P. Kienle, Eds., *The Rudolf Mössbauer Story* (Springer, 2012).

2. R. Röhlsberger, *Nuclear Condensed Matter Physics with Synchrotron Radiation* (Springer, 2005).

3. R. V. Pound, G. A. Rebka, Gravitational red-shift in nuclear resonance. *Phys. Rev. Lett.* **3**, 439–441 (1959). doi:10.1103/PhysRevLett.3.439

4. D. C. Champeney, G. R. Isaak, A. M. Khan, Measurement of relativistic time dilatation using the Mössbauer effect. *Nature* **198**, 1186–1187 (1963). doi:10.1038/1981186b0

5. K. C. Turner, H. A. Hill, New experimental limit on velocity-dependent interactions of clocks and distant matter. *Phys. Rev.* **134**, B252–B256 (1964). doi:10.1103/PhysRev.134.B252

6. I. Troyan, A. Gavriliuk, R. Rüffer, A. Chumakov, A. Mironovich, I. Lyubutin, D. Perekalin, A. P. Drozdov, M. I. Eremets, Observation of superconductivity in hydrogen sulfide from nuclear resonant scattering. *Science* **351**, 1303–1306 (2016). doi:10.1126/science.aac8176 Medline

7. J. Lu, T. Wu, K. Amine, State-of-the-art characterization techniques for advanced lithium-ion batteries. *Nat. Energy* **2**, 17011 (2017). doi:10.1038/nenergy.2017.11

8. R. Röhlsberger, K. Schlage, B. Sahoo, S. Couet, R. Rüffer, Collective Lamb shift in single-photon superradiance. *Science* **328**, 1248–1251 (2010). doi:10.1126/science.1187770 Medline

9. R. Röhlsberger, H.-C. Wille, K. Schlage, B. Sahoo, Electromagnetically induced transparency with resonant nuclei in a cavity. *Nature* **482**, 199–203 (2012). doi:10.1038/nature10741 Medline

10. F. Vagizov, V. Antonov, Y. V. Radeonychev, R. N. Shakhmuratov, O. Kocharovskaya, Coherent control of the waveforms of recoilless γ-ray photons. *Nature* **508**, 80–83 (2014). doi:10.1038/nature13018 Medline

11. K. P. Heeg, H.-C. Wille, K. Schlage, T. Guryeva, D. Schumacher, I. Uschmann, K. S. Schulze, B. Marx, T. Kämpfer, G. G. Paulus, R. Röhlsberger, J. Evers, Vacuum-assisted generation and control of atomic coherences at x-ray energies. *Phys. Rev. Lett.* **111**, 073601 (2013). doi:10.1103/PhysRevLett.111.073601 Medline

12. K. P. Heeg, J. Haber, D. Schumacher, L. Bocklage, H.-C. Wille, K. S. Schulze, R. Loetzsch, I. Uschmann, G. G. Paulus, R. Rüffer, R. Röhlsberger, J. Evers, Tunable subluminal propagation of narrow-band x-ray pulses. *Phys. Rev. Lett.* **114**, 203601 (2015). doi:10.1103/PhysRevLett.114.203601 Medline

13. K. P. Heeg, C. Ott, D. Schumacher, H.-C. Wille, R. Röhlsberger, T. Pfeifer, J. Evers, Interferometric phase detection at x-ray energies via Fano resonance control. *Phys. Rev. Lett.* **114**, 207401 (2015). doi:10.1103/PhysRevLett.114.207401 Medline

14. T. E. Glover, D. M. Fritz, M. Cammarata, T. K. Allison, S. Coh, J. M. Feldkamp, H. Lemke, D. Zhu, Y. Feng, R. N. Coffee, M. Fuchs, S. Ghimire, J. Chen, S. Shwartz, D. A. Reis, S. E. Harris, J. B. Hastings, X-ray and optical wave mixing. *Nature* **488**, 603–608 (2012). doi:10.1038/nature11340 Medline

15. S. Shwartz, M. Fuchs, J. B. Hastings, Y. Inubushi, T. Ishikawa, T. Katayama, D. A. Reis, T. Sato, K. Tono, M. Yabashi, S. Yudovich, S. E. Harris, X-ray second harmonic generation. *Phys. Rev. Lett.* **112**, 163901 (2014). doi:10.1103/PhysRevLett.112.163901 Medline

16. K. Tamasaku, E. Shigemasa, Y. Inubushi, T. Katayama, K. Sawada, H. Yumoto, H. Ohashi, H. Mimura, M. Yabashi, K. Yamauchi, T. Ishikawa, X-ray two-photon absorption competing against single and sequential multiphoton processes. *Nat. Photonics* **8**, 313–316 (2014). doi:10.1038/nphoton.2014.10

17. G. C. Baldwin, J. C. Solem, Recoilless gamma-ray lasers. *Rev. Mod. Phys.* **69**, 1085–1118 (1997). doi:10.1103/RevModPhys.69.1085

18. E. V. Tkalya, Proposal for a nuclear gamma-ray laser of optical range. *Phys. Rev. Lett.* **106**, 162501 (2011). doi:10.1103/PhysRevLett.106.162501 Medline

19. P. Helistö, I. Tittonen, M. Lippmaa, T. Katila, Gamma echo. *Phys. Rev. Lett.* **66**, 2037–2040 (1991). doi:10.1103/PhysRevLett.66.2037 Medline

20. P. Schindelmann, U. van Bürck, W. Potzel, G. V. Smirnov, S. L. Popov, E. Gerdau, Y. V. Shvyd'ko, J. Jäschke, H. D. Rüter, A. I. Chumakov, R. Rüffer, Radiative decoupling and coupling of nuclear oscillators by stepwise Doppler-energy shifts. *Phys. Rev. A* **65**, 023804 (2002). doi:10.1103/PhysRevA.65.023804

21. R. N. Shakhmuratov, F. Vagizov, O. Kocharovskaya, Radiation burst from a single γ-photon field. *Phys. Rev. A* **84**, 043820 (2011). doi:10.1103/PhysRevA.84.043820

22. D.-W. Wang, H.-T. Zhou, M.-J. Guo, J.-X. Zhang, J. Evers, S.-Y. Zhu, Optical diode made from a moving photonic crystal. *Phys. Rev. Lett.* **110**, 093901 (2013). doi:10.1103/PhysRevLett.110.093901 Medline

23. D. Mukhopadhyay, D. A. Walko, I. W. Jung, C. P. Schwartz, J. Wang, D. López, G. K. Shenoy, X-ray photonic microsystems for the manipulation of synchrotron light. *Nat. Commun.* **6**, 7057 (2015). doi:10.1038/ncomms8057 Medline

24. See supplementary materials.

25. C. Ott, A. Kaldun, P. Raith, K. Meyer, M. Laux, J. Evers, C. H. Keitel, C. H. Greene, T. Pfeifer, Lorentz meets Fano in spectral line shapes: A universal phase and its laser control. *Science* **340**, 716–720 (2013). doi:10.1126/science.1234407 Medline

26. R. N. Shakhmuratov, F. G. Vagizov, V. A. Antonov, Y. V. Radeonychev, M. O. Scully, O. Kocharovskaya, Transformation of a single-photon field into bunches of pulses. *Phys. Rev. A* **92**, 023836 (2015). doi:10.1103/PhysRevA.92.023836

27. Y. V. Radeonychev, V. A. Antonov, F. G. Vagizov, R. N. Shakhmuratov, O. Kocharovskaya, Conversion of recoilless γ radiation into a periodic sequence of short intense pulses in a set of several sequentially placed resonant absorbers. *Phys. Rev. A* **92**, 043808 (2015). doi:10.1103/PhysRevA.92.043808

28. P. Schindelmann, thesis, Technische Universität München, Allensbach (1999).

29. R. N. Shakhmuratov, F. Vagizov, O. Kocharovskaya, Single gamma-photon revival from sandwich absorbers. *Phys. Rev. A* **87**, 013807 (2013). doi:10.1103/PhysRevA.87.013807

30. A. Weiner, *Ultrafast Optics* (Wiley, 2009).

31. P. Reiser, thesis, Ruprecht-Karls-Universität Heidelberg (2014).

32. W. Sturhahn, *Hyperfine Interact.* **125**, 149–172 (2000). doi:10.1023/A:1012681503686

33. T. Pfeifer, Y. Jiang, S. Düsterer, R. Moshammer, J. Ullrich, Partial-coherence method to model experimental free-electron laser pulse statistics. *Opt. Lett.* **35**, 3441–3443 (2010). doi:10.1364/OL.35.003441 Medline

34. H.-C. Wille, H. Franz, R. Röhlsberger, W. A. Caliebe, F.-U. Dill, Nuclear resonant scattering at PETRA III: Brillant opportunities for nano – and extreme condition science. *J. Phys. Conf. Ser.* **217**, 012008 (2010). doi:10.1088/1742-6596/217/1/012008

35. R. Rüffer, A. I. Chumakov, Nuclear resonance beamline at ESRF. *Hyperfine Interact.* **97-98**, 589–604 (1996). doi:10.1007/BF02150199